SLAC-PUB-6689
October 1994
(A)

A PPM-Focused Klystron At X-Band With a Travelling-Wave Output Structure*

Kenneth R. Eppley
Stanford Linear Accelerator Center
PO Box 4349, Stanford, California, 94309

Abstract. We have developed algorithms for designing disk-loaded travelling-wave output structures for X-band klystrons to be used in the SLAC NLC. We use either a four- or five-cell structure in a $\pi/2$ mode. The disk radii are tapered to produce an approximately constant gradient. The matching calculation is not performed on the tapered structure, but rather on a coupler whose input and output cells are the same as the final cell of the tapered structure, and whose interior cells are the same as the penultimate cell in the tapered structure. 2-D calculations using CONDOR model the waveguide as a radial transmission line of adjustable impedance. 3-D calculations with MAFIA model the actual rectangular waveguide and coupling slot. A good match is obtained by adjusting the impedance of the final cell. In 3-D, this requires varying both the radius of the cell and the width of the aperture. When the output cell with the best match is inserted in the tapered structure, we obtain excellent cold-test agreement between the 2-D and 3-D models. We use hot-test simulations with CONDOR to design a structure with maximum efficiency and minimum surface fields. We have designed circuits at 11.424 Ghz for different perveances. At 440 kV, microperveance 1.2, we calculated 81 MW, 53 percent efficiency, with peak surface field 76 MV/m. A microperveance 0.6 design was done using a PPM stack for focusing. At 470 kV, 193 amps, we calculated 58.7 MW, 64.7 percent efficiency, peak surface field 62.3 MV/m. At 500 kV, 212 amps, we calculated 67.1 MW, 63.3 percent efficiency, peak surface field 66.0 MV/m.

INTRODUCTION

The NLC design at SLAC requires a klystron producing 50 MW peak power at 11.424 GHz with a pulse length of 1.5 microseconds. A single gap output cavity would break down under these conditions. An extended output circuit should provide lower gradients and potentially higher efficiency. We have studied several disk-loaded travelling-wave output circuits at SLAC. Our main design tools have been the 1-D TWT code HARMON, the 2-D EM code URMEL, the2-D magnetostatic code POISSON, the 2-D PIC code CONDOR, and the 3-D EM code MAFIA. CONDOR models the buncher cavities using the port approximation [3]. In the output section it models the actual geometry of the disks. The coupling to the waveguide is imposed as a port boundary condition on the outer wall of the last cell. This behaves like a radial transmission line with adjustable impedance. We can also adjust the coupling by

Work supported by Department of Energy contract DE–AC03–76SF00515.

⋆ Work supported by Department of Energy contract DE–AC03–76SF00515.

adding a reactive phase to the impedance, or alternately tune the output cell by adjusting its dimensions.

CONSTANT GRADIENT $\pi/2$ STRUCTURE

Our travelling-wave output structures have been four- or five-cell, disk-loaded structures, with a $\pi/2$ phase shift and with varying disk radii to maintain an approximately constant gradient for all cells (Figure 1). These structures have a broad bandwidth. This is not essential for the NLC, but is useful because the circuit is less sensitive to small changes in the dimensions. The coupling to the waveguide is through an iris in the last cell.

Matching is done using a five-cell structure with input and output couplers on the ends, and three identical inner cells (Figure 2). The end cells correspond to the last cell of the tapered structure and the inner cells to the next to last cell. We use the same five-cell coupler with both CONDOR and MAFIA. With MAFIA, the radius of the coupler cell and the aperture of the iris are varied to obtain the best match. With CONDOR, the radius and the impedance of the port are varied. In all cases the input and output cells are identical. The mesh used in MAFIA was relatively coarse, with only six points modelling the rounded end of the disk. We obtained very good agreement between the 2-D and 3-D field distribution, with amplitudes agreeing to about 10 percent (normalized to the power level) and phases agreeing to better than 0.1 radian (Figure 3). CONDOR calculations used both this mesh and a mesh three times finer for comparison. Hot- and cold-test results were similar for both mesh sizes.

Our cold-test calculations initially used a single antenna, ususally on axis or across one of the cavity gaps. We discovered that a volume phased array of antennas can give a much better approximation to the behavior of a beam. The array extends over a cylinder with radius equal to the beam, with constant radial current density. The phases change with phase velocity equal to the beam velocity. A further refinement is to taper this velocity, assuming a linear variation in beam energy through the circuit. The current can also be tapered linearly.

We also used a current array with the amplitude and phase distribution produced by the simulation with the beam (but with constant radial current density). The result agreed very closely to the full beam simulation. This calculation is much faster than the particle simulation. It is useful in checking the results with a finer mesh, and may be used for 3-D simulations with MAFIA.

DESIGN OF THE PPM STACK

After extensive parameter studies to optimize efficiency with minimal surface fields, we have obtained designs for several values of perveance. At microperveance 1.2 (350 amps, 440 kV), the code predicts 53 percent efficiency (81 MW) with peak surface field of 76 MV/m (including 3-D asymmetries). This design will be tested in the SLAC XL3 (Figure 4). At microperveance 0.8 (290 amps, 440 kV), we calculate 60 MW, 58 percent efficiency, peak field 67 MV/m. At microperveance 0.6 (190 amp, 465 kV), we calculate 55 MW, 62 percent efficiency, peak field 63 MV/m. The 0.6 design was also redone with a periodic permanent magnet (PPM) stack replacing the solenoid (Figure 5). An electromagnet would use an unacceptably high average power unless it were superconducting. The lower perveance design is much easier to focus using PPM as well as having higher efficiency. The permanent magnet design had similar efficiency to the solenoid (193 amps, 470 kV, 58.7 MW, 64.7 percent efficiency, 62.3 MV/m peak field). The slightly better results for PPM were due to the hollower beam giving better coupling to the circuit.

The design took into account the constraints on the cavity locations required by the magnet pole pieces. For the buncher section, a standard periodic array of alternating sign magnets worked well in simulation. The magnets for the disk-loaded structure itself could not maintain the same periodicity as the rest of the stack. Initially, two long period magnets were tried there. It was found that having a field reversal in the output strucure or the tailpipe always resulted in expansion of the beam, and sometimes reflection of particles. The best results were obtained using one basically continuous magnet (of tapered strength) in the output structure and tailpipe, with the final pole piece at the beginning of the collector (Figure 6). Initially we tried a completely axisymmetric design, leaving a gap for the output waveguide. However, this would have required magnets whose size was impractically large. We decided to permit a deviation from axisymmetry by cutting slots for the waveguides to exit. The slots reduce the effective magnet strength by about 10 to 20 percent. To prevent a dip in the field at this point, iron flux rings were added, approximately at the center of the magnets on either side of the waveguide, on the inner radius. By adjusting these rings, it was possible to get a field distribution which was almost flat across the waveguide location. Simulations with this field showed a good margin of clearance throughout the structure, with a fill factor of 75 percent or less (Figure 7). Beam stay-clear at 3 db above saturation was almost as good. There were no reflected particles.

It was possible to keep the magnet energy product below $2.4 \cdot 10^7$ Gauss-Oersted, which is not difficult to obtain commercially with Samerium-Cobalt, by enlarging the magnet radii. The largest was in the output structure, with an outer radius of 5.33 cm and an inner radius of 2.15 cm. With Neodymium-Boron-Iron magnets, an energy product of up to $3.5 \cdot 10^7$ Gauss-Oersted is obtainable, permitting smaller, less expensive magnets. This material is more sensitive to temperature, which would make necessitate more elaborate cooling.

The same design, run with a gun voltage of 500 kV, 212 amps, predicted 67.1 MW, 63.3 percent efficiency, peak surface field 66.0 MV/m. Beam stay-clear was similar to that at 470 kV. Because the gun housing does not need to fit through the bore of an electromagnet, we have increased the spacing of the elements in the gun. The resultant gradients are low enough that gun is expected to work without difficulty at 500 kV.

The PPM-focused tube will be tested in the SLAC XL4.

RECTANGULAR OUTPUT CAVITY

According to MAFIA calculations, the azimuthal asymmetry due to the coupling iris in the last cell can increase the peak fields by 20 to 30 percent. We can reduce this problem by making the final cavity with a non-circular cross section (Figure 8). We compensate for the asymmetry by reducing the radius near the iris and increasing the radius in the other direction. An elliptical cross section worked well, but a rectangular cross section turned out to be just as effective and simpler to design and build. With proper dimensions, we can keep a good match while reducing the azimuthal asymmetry to 6 percent.

FINE-TUNING THE COMPUTATIONAL MESH

The coarseness of the computational mesh can present problems in producing a laboratory structure with the same rf properties as in the simulation. We have improved the accuracy of the simulation by partial filling the outer mesh line of the cells, giving an order of magnitude better resolution of the cell radii. We restrict the z dimensions as built to be identical to those used in the simulation. To better calculate the rounded ends of the disks, which are poorly modelled in the simulation, we use SUPERFISH with a fine mesh to model a single disk and its two neighboring cells. We adjust the disk inner radius to give the same frequencies as those found in the coarse mesh simulation. With these techniques, the measured cold-test data agreed to within 10 MHz of the simulation with no output coupling. With coupling, the agreement was within 50 MHz. The bandwidth of the structure is large enough that this difference is not expected to change the hot behavior significantly.

STABILITY ANALYSIS

If an extended-output circuit has a mode with a negative beam-loaded conductance, and the external Q for this mode is greater than the absolute value of the beam-loaded Q, the structure may oscillate in this mode. A semi-analytic analysis using SUPERFISH calculations of the modes for the XL3 (with output shorted) predicted a negative beam loading for the $3\pi/4$ mode, with a beam-loaded Q of -621 at 440 kV. The SUPERFISH frequency for the mode was 11.8 GHz. CONDOR simulations gave a lower frequency for the mode (11.6 GHz). CONDOR simulations of the output structure with an unmodulated beam, run for about 200 ns, showed a high amplitude oscillation at this frequency if the external Q was 680, but this saturated at a low level if the external Q was 630 (Figure 9). The actual external Q at this frequency is expected to be considerably lower than 600. (The Q at the operating frequency when matched is about 40.)

EXPERIMENTAL RESULTS

Cold-test results on the XL3 output circuit are in reasonable agreement with the simulations. So far, the only hot-test results are for the XL1, which was a standing-wave, rather than a traveling-wave structure. However, the comparison to CONDOR simulation does provide a test of the accuracy of the disk-loaded model. (These short, strongly coupled structures are in reality hybrids rather than pure standing-wave or travelling-wave circuits.) The XL1 produced 58 MW at 415 kV, 332 amps, for an efficiency of 42.1 percent. CONDOR simulations at the same voltage and current predicted 41.0 percent efficiency, within the experimental uncertainty. The calculated 2-D surface field was 52 MV/m, which was probably increased to between 60 to 70 MV/m by the asymmetry of the coupling slot. This tube was able to produce over 50 MW with a pulse length of 1.5 microseconds. It was necessary to readjust the magnetic field at longer pulses to eliminate an oscillation at 17 GHz, and this reduced the efficiency somewhat. The oscillation is believed to be due to a TE mode in the last three buncher cavities. The XL2 has been redesigned to eliminate the oscillation.

CONCLUSIONS

It is possible to represent a disk-loaded output structure reasonably well with a 2-D model, if one couples the waveguide to a cylindrical cell through an iris, uses a broad band circuit, and uses 3-D modelling to verify the field patterns. We have designed several circuits using a $\pi/2$ mode tapered to give a constant gradient which simulations predict will give high efficiency with moderate gradients.

REFERENCES

1. B. Aiminetti, S. Brandon, K. Dyer, J. Moura, and D. Nielsen, Jr., *CONDOR User's Manual,* Livermore Computing Systems Document (Lawrence Livermore National Laboratory, Livermore, CA., April, 1988).

2. T. Weiland et al., "MAFIA, Das universelle Software-System fur elecktromagnetisches CAD," the MAFIA Collaboration, Darmstadt, Germany, 1991.

3. K. Eppley, "Algorithms for the Self-Consistent Simulation of High Power Klystrons," SLAC PUB 4622, Stanford Linear Accelerator Center, May 1988.

FIGURE 1. MAFIA simulation of the tapered structure for the XL3.

FIGURE 2. MAFIA simulation of 5 cell coupler used to match the $\pi/2$ structure into the waveguide.

FIGURE 3A. Comparison of MAFIA simulation versus lab measurement of XL3 circuit, frequency response for first cell (on axis), driven from waveguide.

FIGURE 3B. CONDOR simulation of cold-test frequency response of XL3 output circuit, electric field on axis at center of cells, driven from waveguide.

FIGURE 3C. MAFIA simulation of cold-test frequency response of XL3 output circuit, electric field on axis at center of cells, driven from waveguide.

FIGURE 4. CONDOR simulation of $\pi/2$ TW structure for XL3 (perveance 1.2). Electron position space distribution (not to scale) is shown. Horizontal scale is Z, vertical is R. Output section.

FIGURE 5A. CONDOR simulation of $\pi/2$ structure for XL4 (perveance 0.6, PPM focused). Electron position space distribution distribution - low power section (470 kV, 193 amps, saturated drive).

FIGURE 5B. XL4 electron position space distribution distribution - output section.

FIGURE 5C. XL4 RF and DC current - output section.

FIGURE 6A. XL4 BZ on axis from PPM stack - low power section.

FIGURE 6B. XL4 BZ on axis from PPM stack - output section.

FIGURE 6C. XL4 contour plot of magnetic field in output section. Pole pieces and flux rings are shown. (Magnets not shown.)

FIGURE 6D. Schematic of magnet geometry for XL4 output section - side view.

FIGURE 6E. Schematic of magnet geometry for XL4 output section - top view.

FIGURE 7. XL4 time-integrated position space distribution (470 kV, 193 amps, saturated drive) - output section.

FIGURE 8. Side view of the rectangular coupling cavity.

FIGURE 9A. XL3 stability analysis for $3\pi/4$ mode. Beam-loaded Q versus beam voltage.

FIGURE 9B. XL3 stability analysis - frequency spectrum of particle simulation with no external drive, Q external set to 680. Results shown after 200 ns.

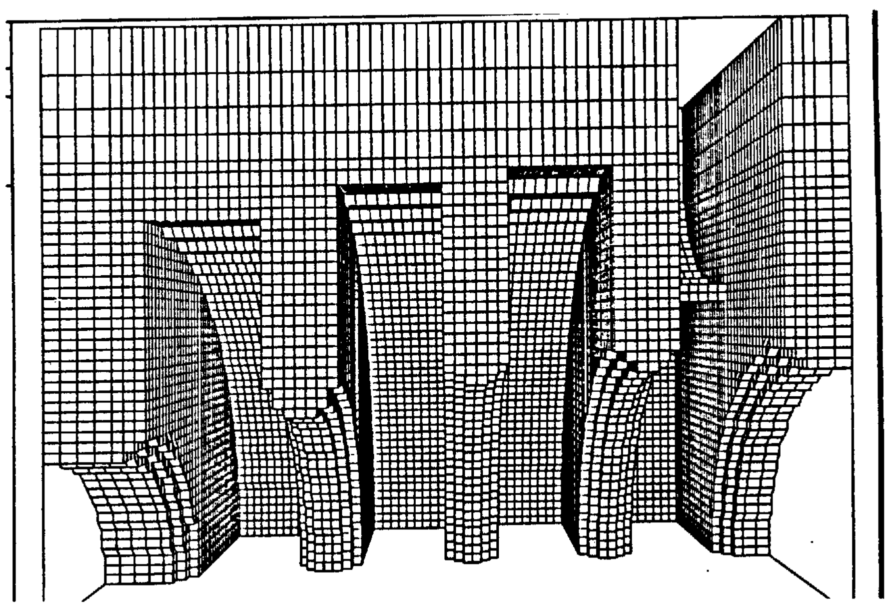

Figure 1

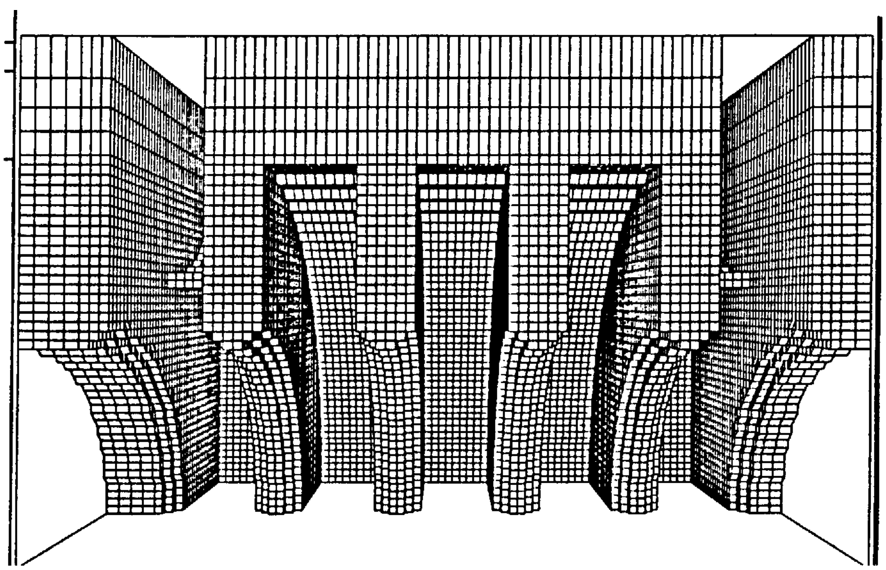

Figure 2

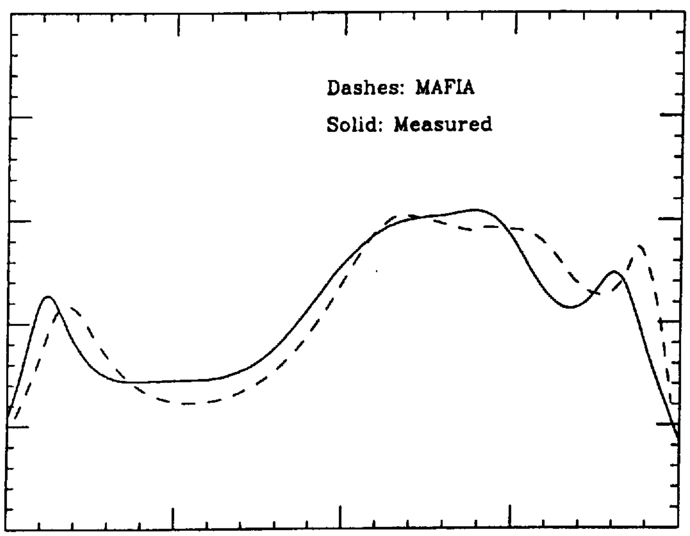

Figure 3a

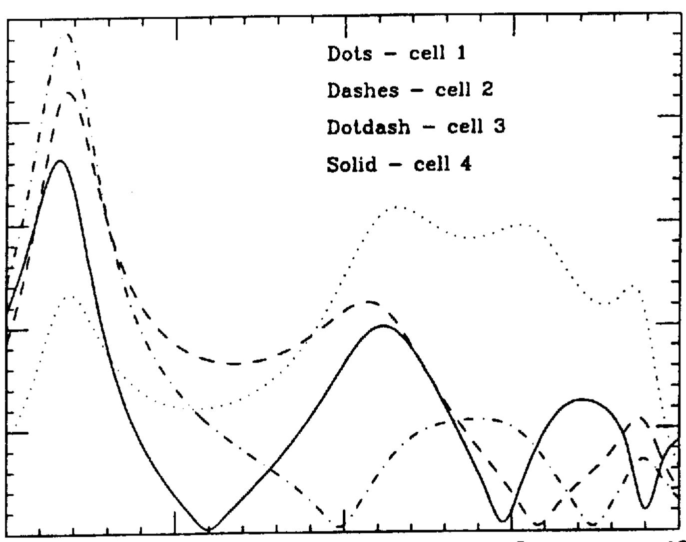

Figure 3b

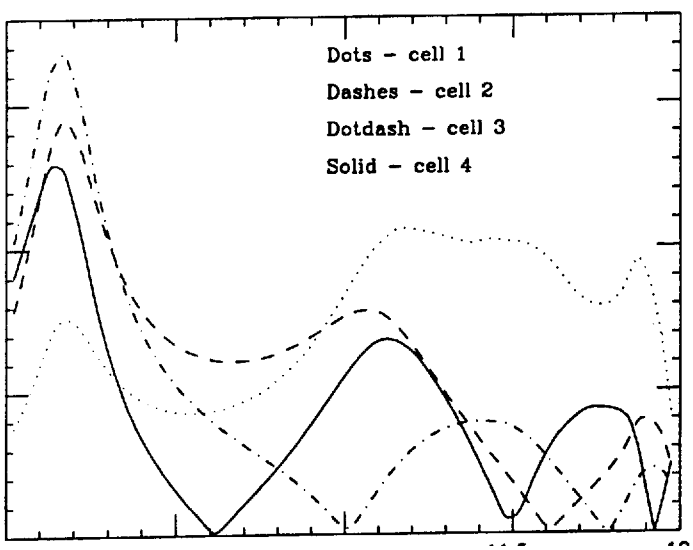

Figure 3c

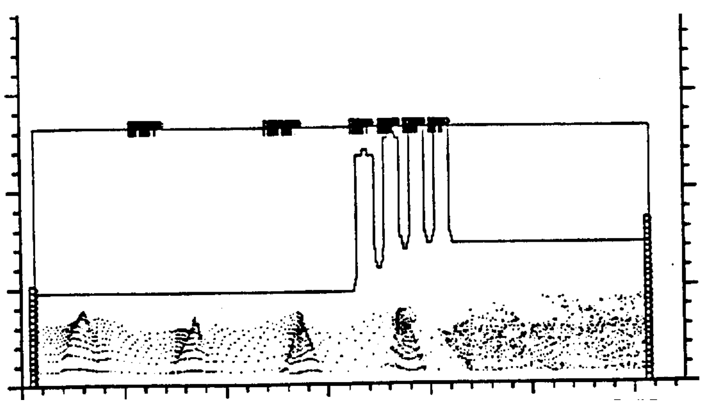

Figure 4

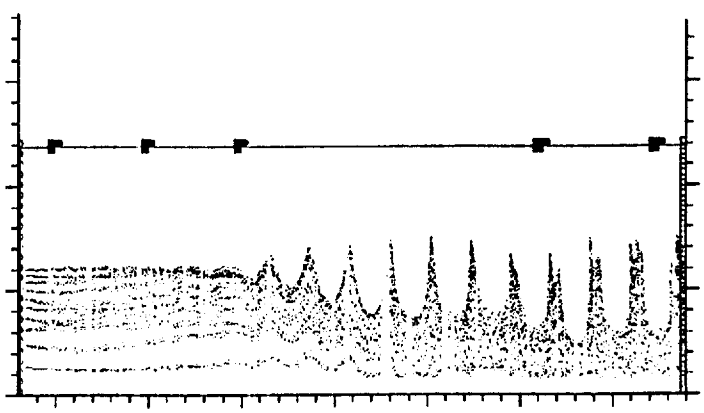

Figure 5a

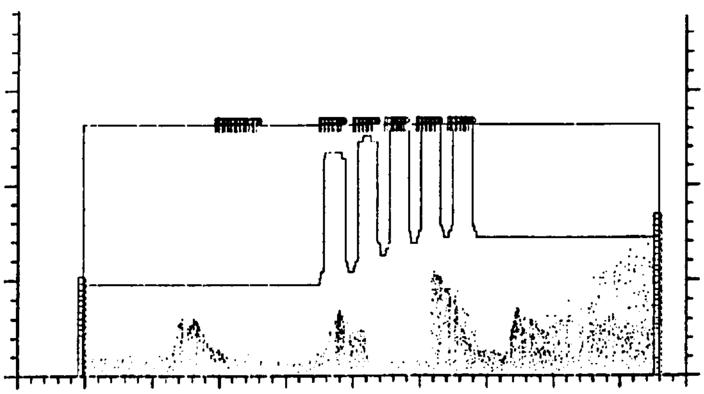

Figure 5b

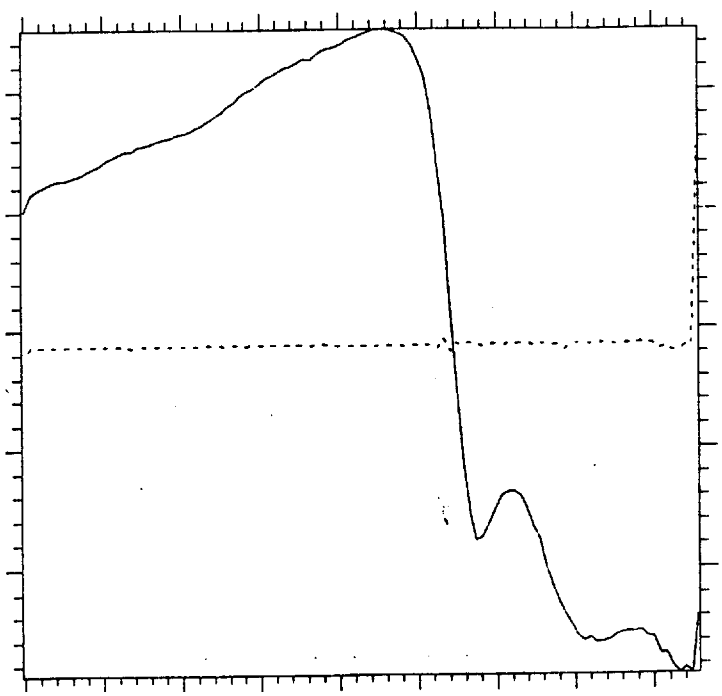

Figure 5c

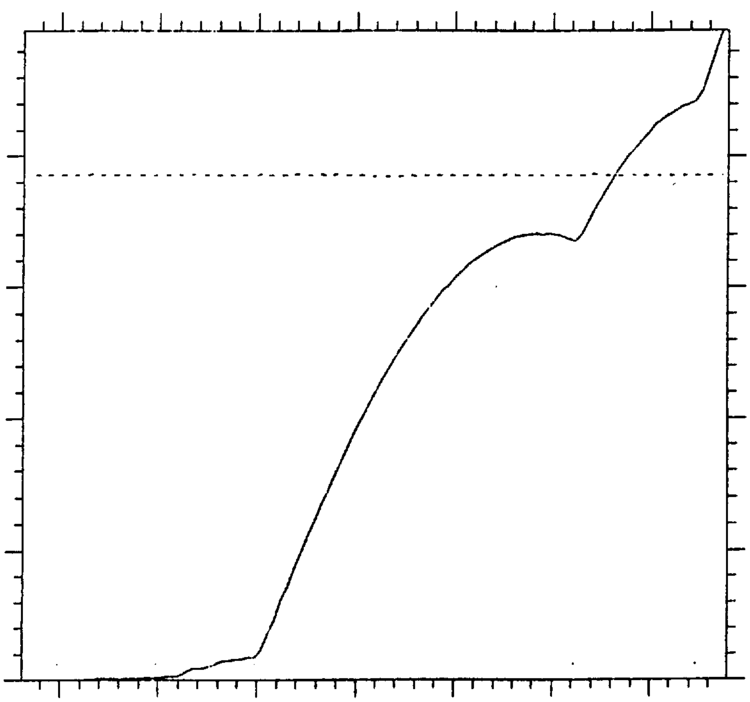

Figure 5e

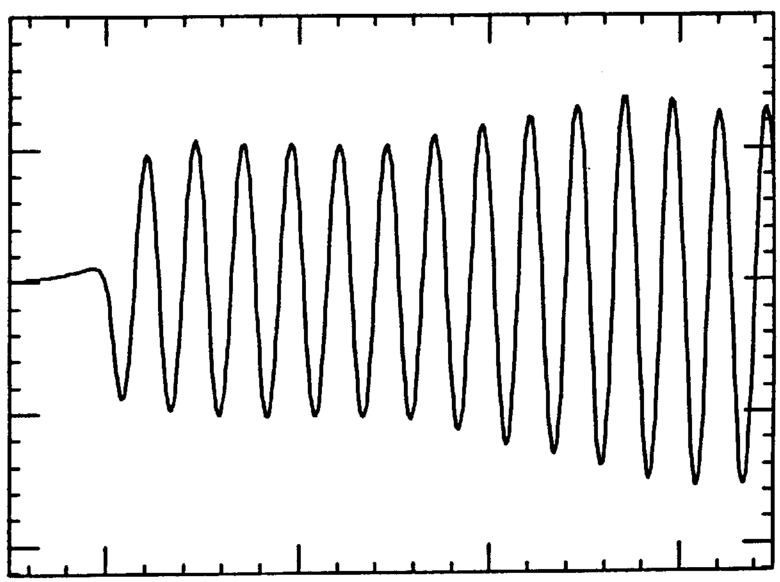

Figure 6a

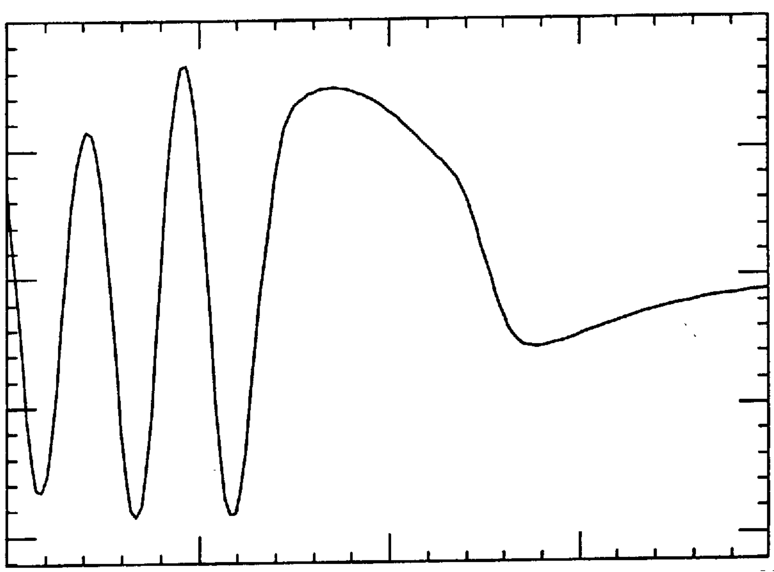

Figure 6b

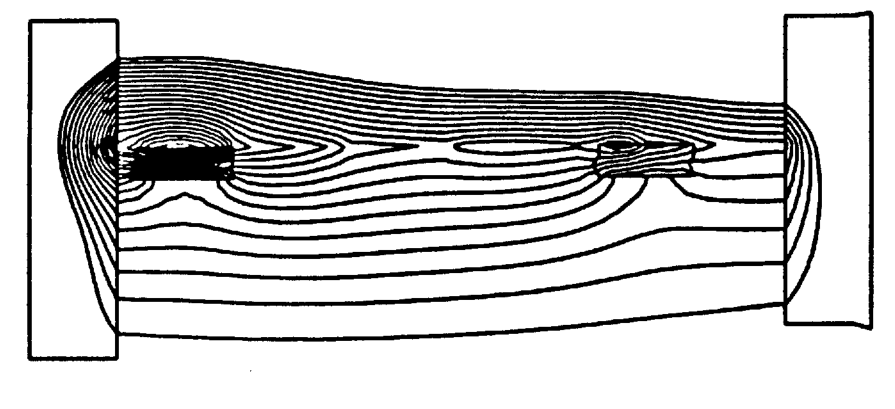

Figure 6c

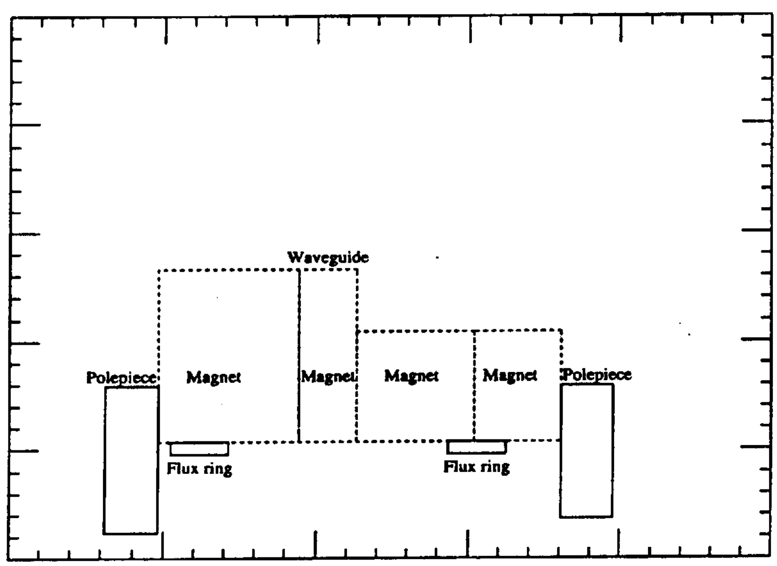
Waveguide
Polepiece
Magnet
Magnet
Magnet
Magnet
Polepiece
Flux ring
Flux ring

Figure 6d

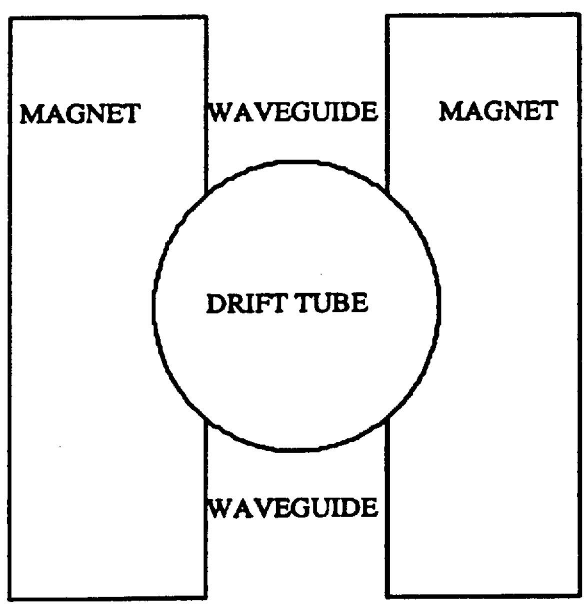

Figure 6e

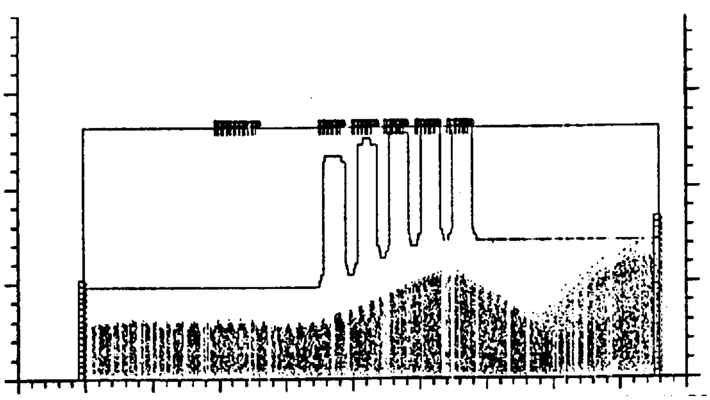

Figure 7

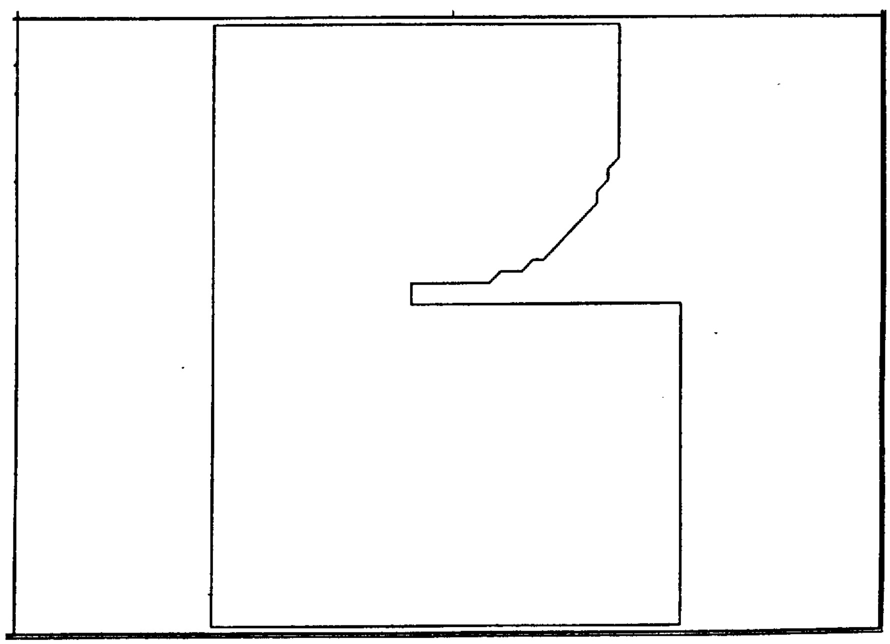

Figure 8

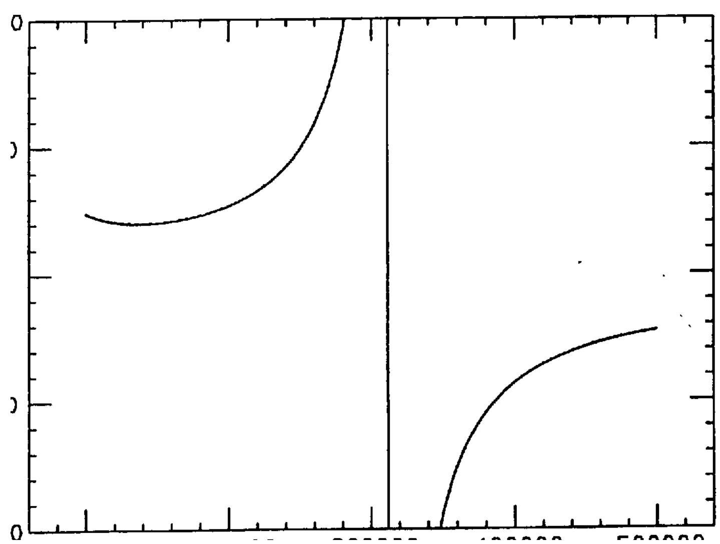

Figure 9a

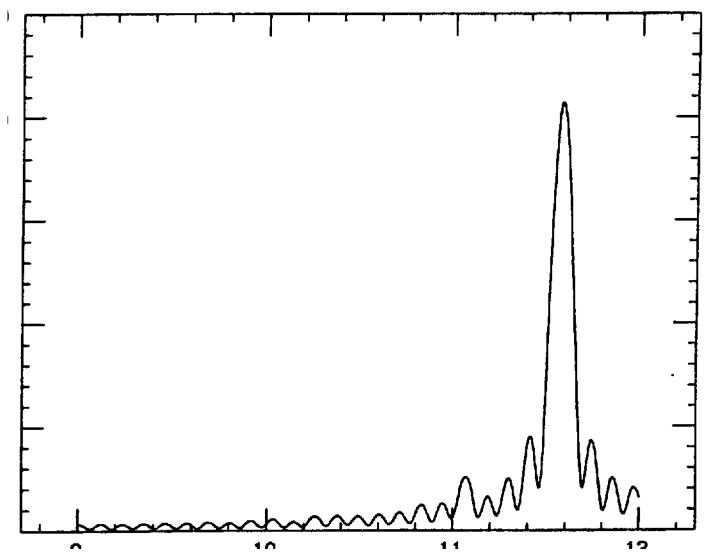

Figure 9b